

Journal of Materials Chemistry A

Accepted Manuscript



This is an *Accepted Manuscript*, which has been through the Royal Society of Chemistry peer review process and has been accepted for publication.

Accepted Manuscripts are published online shortly after acceptance, before technical editing, formatting and proof reading. Using this free service, authors can make their results available to the community, in citable form, before we publish the edited article. We will replace this *Accepted Manuscript* with the edited and formatted *Advance Article* as soon as it is available.

You can find more information about *Accepted Manuscripts* in the [Information for Authors](#).

Please note that technical editing may introduce minor changes to the text and/or graphics, which may alter content. The journal's standard [Terms & Conditions](#) and the [Ethical guidelines](#) still apply. In no event shall the Royal Society of Chemistry be held responsible for any errors or omissions in this *Accepted Manuscript* or any consequences arising from the use of any information it contains.



Journal Name

ARTICLE

Hydrogen absorption–desorption characteristics of a Gd₂Co₇-type Sm_{1.6}Mg_{0.4}Ni₇ compound

Received 00th January 20xx,
Accepted 00th January 20xx

DOI: 10.1039/x0xx00000x

www.rsc.org/

Lu Zhang,^{ab} Yanqiao Ding,^{ab} Yuan Li,^{ab} Yumeng Zhao,^{ab} Xin Zhao,^c Baozhong Liu^{*d} and Shumin Han^{*ab}

In this paper, we reported a new Gd₂Co₇-type Sm_{1.6}Mg_{0.4}Ni₇ compound as hydrogen storage materials with special hydrogen absorption/desorption process and good hydrogen storage ability. The Gd₂Co₇-type Sm_{1.6}Mg_{0.4}Ni₇ compound absorbs 1.88 wt% H₂ within 17 min at 298 K under 10 MPa H₂. Meanwhile, the hydrogen absorption speed accelerates to 3.4 min after 20 hydrogenation/dehydrogenation cycles with a 1.44 wt% H₂ under 3 MPa H₂. Especially, the capacity retention rate of the compound reaches 99.3% at the 100th cycle. We found the hydrogen absorption/desorption of the compound undergoes two equilibrium stages, relating to the transformation of H₂ between H-solid solution phase and hydride phase with a lower rate and higher enthalpy change at the lower concentration H₂ stage, and the direct conversion between H₂ and the hydride phase with a higher rate and lower enthalpy change at the higher concentration H₂ stage. The two step mode lowers the inner-molecular strain and mismatch in subunit volumes of the compound in hydrogen absorption/desorption, caused from the transformation of H₂ at the lower concentration of H₂ stage, thus leading to good structural stability and excellent cycling stability. The new insights are expected to provide viable intermetallic materials as high-pressure tank materials for hydrogen storage with nice hydrogen storage properties.

1. Introduction

RE–Mg–Ni-based compounds have been widely studied because of their specific crystal structures, higher discharge capacity and rate discharge performance, and excellent activation behavior in decade.^{1–3} At present most of the researches mainly focused on La–Mg–Ni compounds, including La₂MgNi₉, La₃MgNi₁₄ and La₄MgNi₁₉.^{4–7} These compounds have superlattice structures, where one [LaMgNi₄] and n [LaNi₅] (n = 1, 2 and 3, respectively) subunits stack along the c-axis alternatively according to different patterns, and each superlattice structure crystallizes in two polymorphic forms, namely, a hexagonal 2H structure (CeNi₃-type, Ce₂Ni₇-type and Pr₅Co₁₉-type, respectively) and a rhombohedral 3R-type structure (PuNi₃-type, Gd₂Co₇-type and Ce₅Co₁₉-type, respectively). Mg atoms occupy La sites in Laves-type [LaMgNi₄] subunits rather than those of the [LaNi₅] subunits in the systems.⁴

In year, new type Sm–Mg–Ni compounds are found more interesting, and have attracted increasing attentions due to the

excellent cycling stability after hydrogenation/dehydrogenation. Chen *et al.* found that the hydrogen-induced amorphization and phase decomposition phenomenon did not occur for AB₂-type SmMgNi₄ compound, which was different from the other AB₂-type RE–Mg–Ni compounds,^{8,9} and 84% capacity remained after 50 hydrogenation/dehydrogenation cycles at 298 K.¹⁰ Zhang and co-workers investigated the structural parameters and hydrogen absorption/desorption properties of Sm₂MgNi₉, Sm₃MgNi₁₄ and Sm₄MgNi₁₉ (as well as SmMgNi₄ and SmNi₅ as references) compounds,¹¹ and reported that the superlattice Sm–Mg–Ni compounds not only possessed good hydrogen storage capacity, which were 1.03, 1.04 and 0.93 H/M under 10 MPa at 298 K, but showed superior cycling stability, which the capacity retention rate of the Sm₄MgNi₁₉ was ca. 97% without occurrence of the amorphization and phase decomposition. Hence, the Sm–Mg–Ni compounds are of great research value as a novel intermetallic hydrogen storage material, and understanding on their detailed hydrogen absorption/desorption process is basic and important for further studies on the Sm–Mg–Ni compounds.

Our previous studies on La–Mg–Ni compounds have shown that the compounds with A₂B₇-type superlattice structure exhibit good hydrogen storage properties.^{12,13} However, the compounds tend to form multiphase structure during the preparation process and the existence of the interaction between different superlattice phases can distinctly affect the hydrogen storage properties.^{14,15} Therefore, to understand the specific hydrogen storage properties of the A₂B₇-type La–Mg–Ni compounds, some single phase La–Mg–Ni compounds with Ce₂Ni₇-type superlattice structure have been prepared.^{13,16} While Gd₂Co₇-type La–Mg–Ni compounds have never been

^a State Key Laboratory of Metastable Materials Science and Technology, Yanshan University, Qinhuangdao 066004, PR China.

^b College of Environmental and Chemical Engineering, Yanshan University, Qinhuangdao 066004, PR China.

^c Baotou Research Institute of Rare Earth, Baotou 014030, PR China.

^d School of Materials Science & Engineering, Henan Polytechnic University, Jiaozuo 454000, PR China.

* Corresponding author: Tel & fax: +86-335-8074648, *E-mail address: hanshm@ysu.edu.cn (S. Han), and Tel & fax: +86 335 3989859, *E-mail address: bzliu@hpu.edu.cn (B. Liu).

† Electronic Supplementary Information (ESI) available: [details of any supplementary information available should be included here]. See DOI: 10.1039/x0xx00000x

prepared and reported due to the high temperature modification of the Gd_2Co_7 -type structure, which is unstable in comparison with the Ce_2Ni_7 -type structure at lower temperatures and can easily transform to other phases.^{17–19} Our group recent studies found that the existence of Sm can promote the formation of Gd_2Co_7 -type phase in $\text{La}_{0.60}\text{Sm}_{0.15}\text{Mg}_{0.25}\text{Ni}_{3.4}$ compound, which the phase content reached to 73.2 wt% after annealing 24 hours at 1223 K, and the compound showed good cycling stability.²⁰ Therefore, based on the research, we expect to obtain a Gd_2Co_7 -type Sm–Mg–Ni compound accounting on the effect of Sm to phase structure formation.

In present work, we prepared a Gd_2Co_7 -type Sm–Mg–Ni compound by powder sintering method and studied the hydrogen absorption and desorption properties. We also reveal the special hydrogen absorption/desorption process and its effect on hydrogen storage properties of the Gd_2Co_7 -type Sm–Mg–Ni compound.

2. Experimental

2.1. Preparation of the compound

$\text{Sm}_{1.6}\text{Mg}_{0.4}\text{Ni}_7$ compound was prepared by stepwise sintering technique using precursors: SmNi, MgNi_2 and Ni powders (99.9%). Starting precursors of SmNi and MgNi_2 were prepared by induction melting method in argon atmosphere. Each precursor was remelted three times to ensure homogeneity, and 5 wt% of Sm and 20 wt% of Mg were excessively added to compensate for the losses in the process. All of the precursors were ball milled for 1 h and sieved to below 300 mesh sizes, and then the powder mixtures were cold pressed to a tablet (3 g) under 10 MPa, which subsequently was wrapped in a nickel foil and sintered via a step heating process. To compensate for Mg volatility losses during the sintering process, MgNi_2 was excessively added. Heat treatment involved stepwise rising temperature from room temperature to 873, 973, 1073 K under 0.04 MPa argon atmosphere in the quartz tube (each temperature kept for 1 hour) and then to 1223 K with a sintering time of 96 h. Afterwards, the pellet was cooled to room temperature with the furnace. The as-sintered sample was finally polished to remove the oxide layer and mechanically crushed to powders in a glovebox under argon atmosphere, which the particle size for structural analysis is below 400 meshes, and for property testing is between 200 and 400 meshes.

2.2. Structural and compositional analysis

X-ray diffraction (XRD) measurement was performed on a Rigaku D/Max-2500/PC X-ray diffractometer with Cu $K\alpha$ radiation. Ordinary data for the Rietveld analysis was collected by a step-scan method with measurement conditions: $2\theta = 10\text{--}90^\circ$, 2 s per step, and 0.02° per step. The low angle range XRD pattern was meticulously measured in the 2θ range of 3° to 20° , taking a long time with 4 s per step and 0.02° per step. The degree of the refinement was judged by S : $S = R_{wp}/R_e$, where R_{wp} was the residue of the weighted pattern and R_e was the statistically expected residue value. The chemical composition of the sintered sample was finally examined by inductively coupled plasma (ICP), which indicated a chemical composition of $\text{Sm}_{1.6}\text{Mg}_{0.4}\text{Ni}_7$. Specimen for transmission electron microscopy (TEM) was prepared by mechanical lapping under alcohol then processed by ultrasounding for 30 min. TEM was

performed on JEM-2010 with energy-dispersive X-ray (EDX) operating at 20.0 kV to determine the chemical composition of the sample.

2.3. Hydrogen absorption and desorption measurements

The powder sample (less than 48 μm) of the $\text{Sm}_{1.6}\text{Mg}_{0.4}\text{Ni}_7$ compound with 1.5 g was loaded into stainless steel container and then placed in stainless steel autoclave. The pressure–composition (P – C) isotherms characteristic for the sample were measured at temperatures of 298, 323 and 348 K using the Sieverts' method, respectively. Prior to formal measurements, the alloy sample was firstly held at 298 K under 10 MPa hydrogen atmosphere until the sample was fully hydrogenated. After the sample was activated, the sample was dehydrogenated against a backpressure of 0.0000 MPa for 2 h. The purity of the hydrogen gas was 99.99%. The hydrogen cycling property of the compound was measured at 298 K under 3 MPa hydrogen atmosphere up to 100 cycles. Hydrogen absorption and desorption kinetic measurements during the plateau regions were performed using the method as previous report.²¹

In order to count the hydrogenation and dehydrogenation enthalpy changes of the $\text{Sm}_{1.6}\text{Mg}_{0.4}\text{Ni}_7$ compound, differential scanning calorimetry (DSC) measurement was performed by using a TA instrument, Q20P in a high-purity hydrogen atmosphere. A 9 mg sample was load into the alumina crucible and activated before measurement. The hydrogenated sample was firstly heated with 5 K min^{-1} under 3 MPa initial hydrogen pressure from 323 to 473 K and then cooled with 2 K min^{-1} . The analysis was carried out on the TA Universal Analysis 2000 software.

2.4. Structure analysis of the cycling samples and samples after hydrogenation/dehydrogenation

The structures of the $\text{Sm}_{1.6}\text{Mg}_{0.4}\text{Ni}_7$ compound after 1, 2, 3, 5, 15 and 100 hydrogenation and dehydrogenation cycles were performed by Rietveld refinement. TEM was especially performed on the sample at the 100th hydrogenation/dehydrogenation cycle. To further understand the hydrogen absorption and desorption processes and the effect on lattice structure for the compound, XRD patterns at different hydrogen contents during the processes of the sample were analyzed by Rietveld refinement method in detail.

3. Results and discussion

3.1. Crystal structure

Fig. 1 shows the XRD profile of $\text{Sm}_{1.6}\text{Mg}_{0.4}\text{Ni}_7$ compound, which Gd_2Co_7 -type structure is determined from its characteristic peaks at 32.24° and 34.22° . In regards to the same reflection peak at 33.24° of Ce_2Ni_7 -type and PuNi_3 -type structures, XRD profile of the $\text{Sm}_{1.6}\text{Mg}_{0.4}\text{Ni}_7$ sample in 2θ region between 3° and 15° was performed to identify the impure phase structure. Except for the peaks of the Gd_2Co_7 -type structure of (003 and 006), the reflections of the Ce_2Ni_7 -type structure (002 and 004) are observed, and reflection of the PuNi_3 -type structure (003) does not appear. Therefore, the characteristic peak at 33.24° is part of the Ce_2Ni_7 -type structure. And the compound is composed of Gd_2Co_7 - and Ce_2Ni_7 -type structures.

Fig. 2 shows the Rietveld refinement of the XRD profile of $\text{Sm}_{1.6}\text{Mg}_{0.4}\text{Ni}_7$ compound. The result shows that the content of Gd_2Co_7 -type phase is 96.0 wt%, and that of the Ce_2Ni_7 -type phase is 4.0 wt%. The refined structural parameters of the Gd_2Co_7 -type phase are listed in Table 1. The cell parameters of a , c and V for the Gd_2Co_7 -type phase of $\text{Sm}_{1.6}\text{Mg}_{0.4}\text{Ni}_7$ compound are 4.9462 Å, 35.988 Å and 762.50 Å³, respectively, and those for the Ce_2Ni_7 -type phase are 4.9484 Å, 24.022 Å and 509.40 Å³.

Fig. 3 shows the high resolution TEM (HRTEM) with the corresponding selected area electron diffraction (SAED) pattern after Fast Fourier Transformation (FFT) and the inverse FFT image of the $\text{Sm}_{1.6}\text{Mg}_{0.4}\text{Ni}_7$ compound particle. The [0003] lattice plane of the Gd_2Co_7 -type structure can be determined from Fig. 3a and the stacking mode of the [A₂B₄] and [AB₅] subunit in the ratio of 1:2 is clear in the Fig. 3b. It should be noted that we do not capture the Ce_2Ni_7 -type structure in the TEM analysis, which may be due to the phase abundance of the Ce_2Ni_7 -type phase in the compound is so few in comparison with that of the Gd_2Co_7 -type structure. And because of the same reason, the influence of the Ce_2Ni_7 -type phase on the hydrogen storage properties of $\text{Sm}_{1.6}\text{Mg}_{0.4}\text{Ni}_7$ compound is deemed as that of the Gd_2Co_7 -type phase hereafter in regards to the similar structure and the hydrogen storage properties of the allotrope.

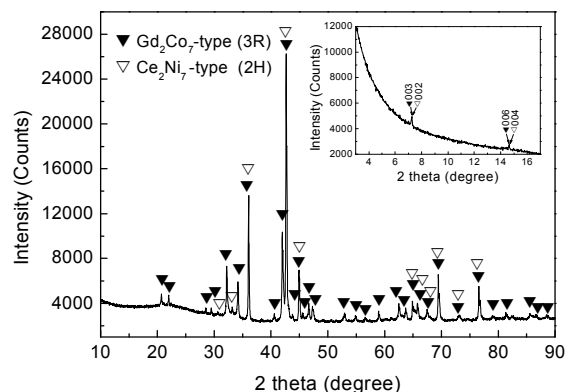


Fig. 1 X-ray diffraction (XRD) profile of the $\text{Sm}_{1.6}\text{Mg}_{0.4}\text{Ni}_7$ compound in 2θ range of 10°–90° and a low angel range of 3°–17°.

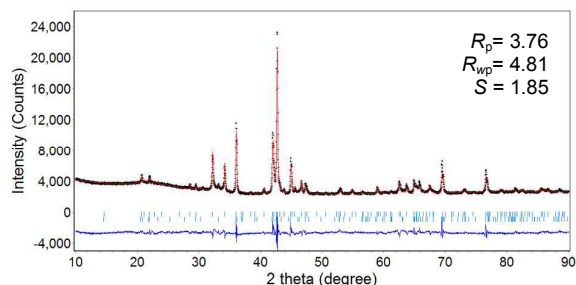


Fig. 2 Rietveld refinement of the $\text{Sm}_{1.6}\text{Mg}_{0.4}\text{Ni}_7$ compound. Vertical bars below the pattern show the positions of all possible reflection peaks of the Gd_2Co_7 -type (3R) and Ce_2Ni_7 -type (2H) phases.

3.2. Hydrogen storage capacity

Fig. 4 shows the activation curve of the Gd_2Co_7 -type $\text{Sm}_{1.6}\text{Mg}_{0.4}\text{Ni}_7$ compound under 10 MPa H_2 at 298 K. It takes ca. 1.5 h to reach a maximum hydrogen content of 1.57 wt% for the activation cycle. After activation process, the sample can store the maximum hydrogen content of 1.88 wt% (1.37 H/M) under the same condition, and it only takes 15 min to store a hydrogen content of 1.58 wt% (1.15 H/M). It can be concluded that the $\text{Sm}_{1.6}\text{Mg}_{0.4}\text{Ni}_7$ compound is easy to be activated and stands out in hydrogen storage capacity.

Table 1 Structural parameters of Gd_2Co_7 -type $\text{Sm}_{1.60}\text{Mg}_{0.40}\text{Ni}_7$ compound, space group R-3m (No. 166), $a = 4.9462$ Å, $c = 35.988$ Å, $V = 762.50$ Å³

Atoms	Sites	x	y	z	Occ.
Sm1	6c ₁	0	0	0.05040	1
Sm2	6c ₂	0	0	0.15521	0.6
Mg	6c ₂	0	0	0.15521	0.4
Ni1	3b ₁	0	0	0.5	1
Ni2	6c ₃	0	0	0.27904	1
Ni3	6c ₄	0	0	0.38801	1
Ni4	9e ₁	0	0	0	1
Ni5	18h ₁	0.50320	-0.50320	0.10959	1

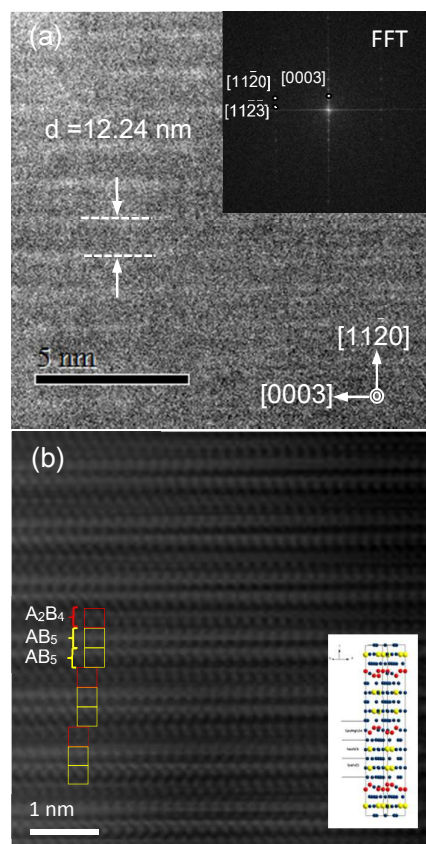


Fig. 3 High-resolution TEM (HRTEM) image with the corresponding SAED pattern after Fast Fourier Transformation (FFT) (a) and inverse FFT image (b) for the crystal grain of the Gd_2Co_7 -type phase in the $Sm_{1.6}Mg_{0.4}Ni_7$ sample.

3.3. Hydrogen absorption kinetics

Fig. 5 shows the hydrogen absorption and desorption curves of the $Sm_{1.6}Mg_{0.4}Ni_7$ sample under 3 MPa H_2 at 298 K for different cycles after activation. The maximum hydrogen content of the compound is 1.45 wt% (1.05 H/M) at the ca. 35 min, and it takes 9.4 min to absorb 90% the maximum hydrogen content for the first hydrogen absorption cycle. During hydrogen desorption, the compound releases 1.44 wt% (1.04 H/M) at the ca. 30 min, and takes ca. 5 min to desorb 90% the maximum hydrogen content for the first cycle. Moreover, the hydrogen absorption and desorption speeds accelerate with cycling, which the slopes of the curves appear more inclined. It only needs 3.4 min to achieve a maximum hydrogen content of 1.44 wt% (1.05 H/M) at the 20th cycle and keeps this hydrogen absorption rate until to the 100th cycle for the hydrogenation, and only needs ca. 1.5 min to fully release the hydrogen at the 20th cycle and speeds to 0.7 min until to the 100th cycle for the dehydrogenation.

3.4. Cyclic property

The cycling stability of the activated $Sm_{1.6}Mg_{0.4}Ni_7$ compound is presented in Fig. 6. The hydrogen retention rate of the compound keeps 99.3% after 100 hydrogenation/dehydrogenation cycles under 3 MPa H_2 at 298 K. The cycling stability of the $Sm_{1.6}Mg_{0.4}Ni_7$ compound is superior in comparison with the previous reported

ternary superlattice compounds of Sm_3MgNi_{14} ,¹¹ Pr_3MgNi_{14} ,²² and

La_4MgNi_{19} ,²³ which are 95%, 98% and 89% after 30 cycles, respectively.

To clarify the degradation mechanism and the good cycling stability of the $Sm_{1.6}Mg_{0.4}Ni_7$ compound under present circumstances, the structures of the fully hydrogenated and dehydrogenated samples after 1, 2, 3, 15 and 100 cycles are examined. The Rietveld refinements of the XRD profiles of the samples are shown in Fig. 7a–j. It can be noticed that no new peak is

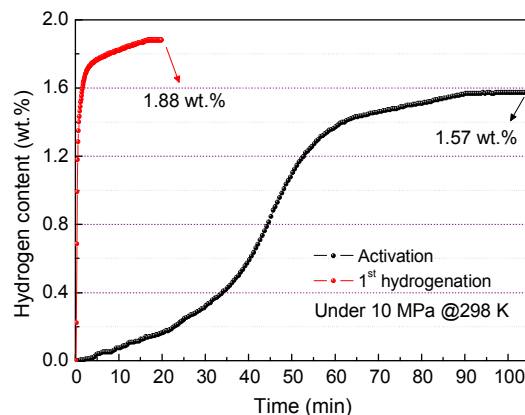


Fig. 4 Activation curve and hydrogen absorption curve for the first cycle of the $Sm_{1.6}Mg_{0.4}Ni_7$ sample under 10 MPa H_2 at 298 K.

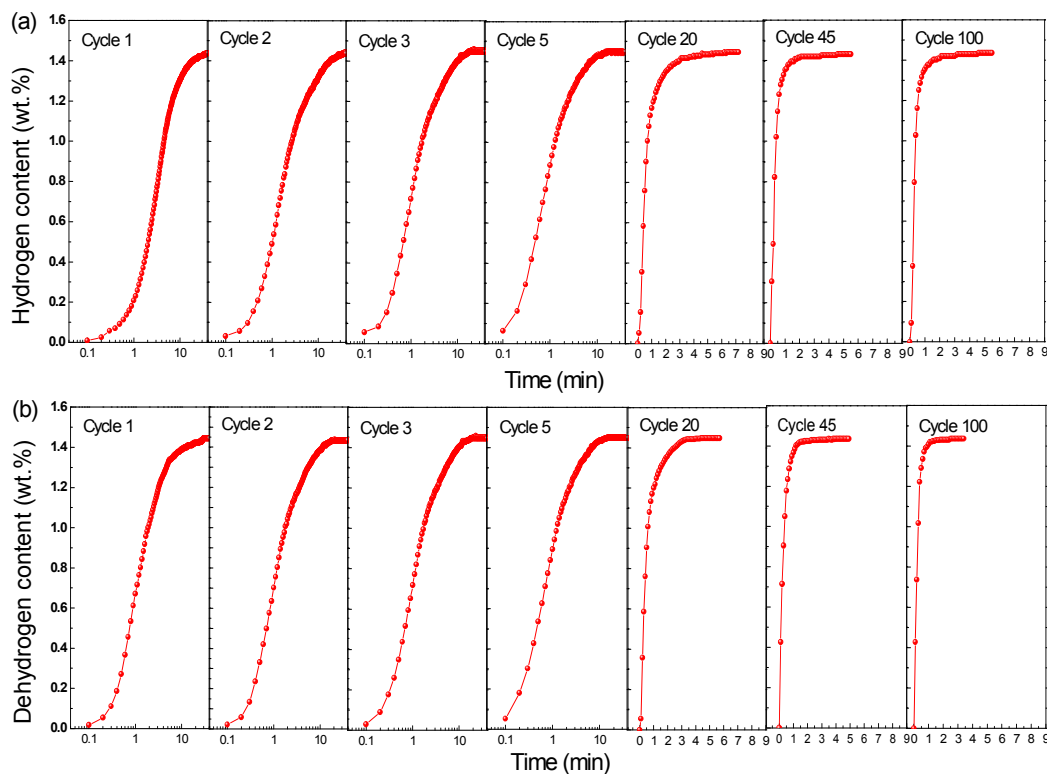


Fig. 5 Hydrogen absorption (a) and (b) desorption curves of the activated $\text{Sm}_{1.6}\text{Mg}_{0.4}\text{Ni}_7$ compound under 3 MPa H_2 at 298 K for the 1st, 2nd, 3rd, 5th, 20th, 45th and 100th cycles.

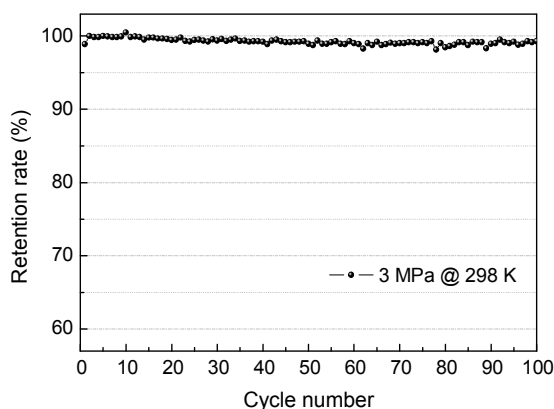


Fig. 6 Cycling stability of the $\text{Sm}_{1.6}\text{Mg}_{0.4}\text{Ni}_7$ compound under 3 MPa H_2 at 298 K.

observed for the fully hydrogenated samples, but all peaks of the hydrogenated samples move left and have broadened (Fig. 7a, c, e, g and i), indicating that no new substance forms and the cell volume of the structure becomes larger due to hydrogenation. And after dehydrogenation, the diffraction peaks of the samples keep almost unchanged without appearance of new peak (Fig. 7b, d, f, h and j). Besides, the SAED pattern of the sample after 100

hydrogenation/dehydrogenation cycles shows that the sample still have a complete lattice structure without appearance of amorphous rings (Fig. 8). The above results indicate that neither disproportionation nor amorphization occurs after hydrogenation/dehydrogenation. Generally, hydrogen storage capacity degradation of superlattice RE–Mg–Ni compounds is mainly related to the formation of dislocation or distortion, and the occurrence of partial disproportionation or amorphization during cycles.^{11,16,24,25} Hence, based on the above results, the formation of dislocation may be the important cause of the capacity degradation because the accumulation of dislocation can lead to the enlargement of lattice strain,^{26,27} which will be discussed below.

Fig. 9 shows the $[\text{A}_2\text{B}_4]$ and $[\text{AB}_5]$ subunit volumes and their changes after hydrogenation and dehydrogenation at the 1–100 cycles, as well as the lattice strain of the $\text{Sm}_{1.6}\text{Mg}_{0.4}\text{Ni}_7$ compound, calculated from the refined XRD profile parameters. The original volume of the $[\text{A}_2\text{B}_4]$ subunit is larger than that of the $[\text{AB}_5]$ subunit, which is 87.02 \AA^3 and 83.57 \AA^3 , respectively. After the first hydrogenation process, the volumes of the $[\text{A}_2\text{B}_4]$ and $[\text{AB}_5]$ subunits expand to 111.6 \AA^3 and 104.9 \AA^3 , and keep within the range of $104.8\text{--}106.0 \text{ \AA}^3$ and $110.3\text{--}111.6 \text{ \AA}^3$ with cycling, respectively (Fig. 9a). After dehydrogenation, the volumes of the $[\text{A}_2\text{B}_4]$ and $[\text{AB}_5]$ subunits shrink to lower values than the original state, which are within the range of $84.52\text{--}85.51 \text{ \AA}^3$ and $82.74\text{--}83.65 \text{ \AA}^3$ with cycling. Fig. 9b shows the volume changes of the $[\text{A}_2\text{B}_4]$ and $[\text{AB}_5]$

subunits based on the last state within the first four cycles. It is clear that the volume expansion and contraction rates of the $[A_2B_4]$ subunit are all larger than that of the $[AB_5]$ subunit, but the rates of two subunits change little with the increase of hydrogenation/dehydrogenation cycles, which the difference of two subunits keep ca. 3.37% and 2.70% for hydrogenation and dehydrogenation, respectively. The above results indicate that the Gd_2Co_7 -type structure of the $Sm_{1.6}Mg_{0.4}Ni_7$ compound is with good restorability and stability. Therefore, disproportionation or amorphization did not appear for the structure. However, accumulation of lattice strain is observed in Fig. 9c. The initial lattice strain of the sample is 0.093%, while the lattice strain firstly increases to the maximum values of 0.413% and 0.140% at the 2nd hydrogenation and dehydrogenation cycles, and then decreases to stable values of ca. 0.38% and 0.13% with further rising cycles for hydrogenation and dehydrogenation, respectively. The accumulation lattice strain after hydrogenation and dehydrogenation process relates to the subunit changes of the crystal structure, namely the formation of dislocation or distortion of the crystal structure. Hence it can be concluded that the formation of the dislocation or distortion of the crystal structure is the dominant factor for degradation in hydrogen storage capacity, similar to the reported $Pr_{0.6}Mg_{1.4}Ni_4$ ²⁷ and V-Ti compounds.²⁸

reflection peaks of the Ce_2Ni_7 -type (2H) and Gd_2Co_7 -type (3R) phases for A, and 3R and 2H phases for D.

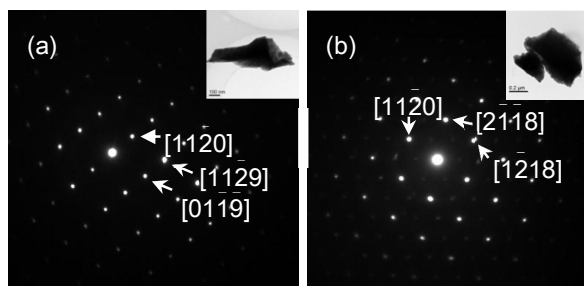


Fig. 8 SAED patterns of the Gd_2Co_7 -type structure for the original (a) and after 100 hydrogenation/dehydrogenation cycles (b) of the $Sm_{1.6}Mg_{0.4}Ni_7$ compound.

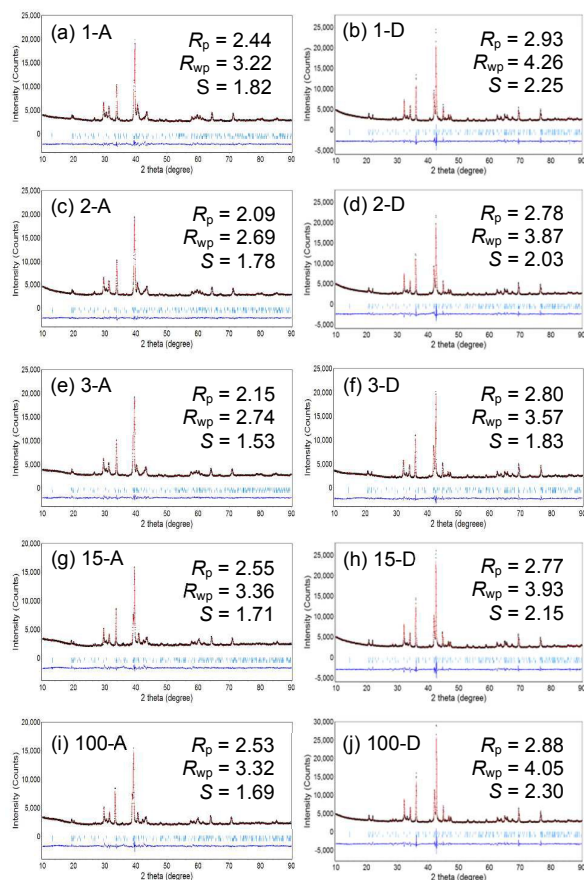


Fig. 7 Rietveld refinements of the hydrogenated (A) and dehydrogenated (D) $Sm_{1.6}Mg_{0.4}Ni_7$ compound after 1 cycles (a, b), 2 cycles (c, d), 3 cycles (e, f), 15 cycles (g, h) and 100 cycles (i, j). Vertical bars below the pattern show the positions of all possible

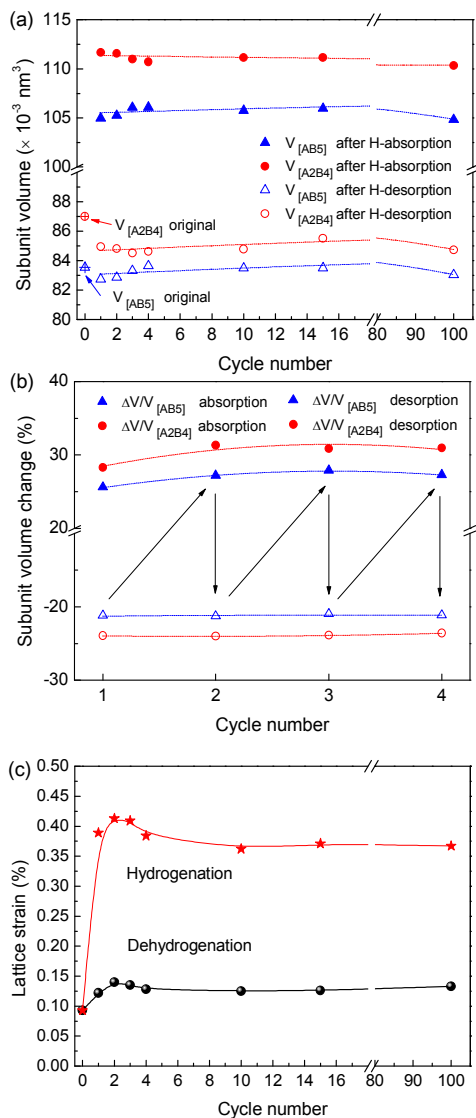


Fig. 9 Subunit volume (a) and subunit volume change (b) of the [A₂B₄] and [AB₅] subunits of the Sm_{1.6}Mg_{0.4}Ni₇ compound after hydrogenation and dehydrogenation at different cycles. Lattice strain after hydrogenation/dehydrogenation at different cycles of the Sm_{1.6}Mg_{0.4}Ni₇ compound (c).

3.5. Hydrogen absorption–desorption thermodynamics

To study the hydrogen absorption and desorption thermodynamics, the P – C isotherms of the activated Sm_{1.6}Mg_{0.4}Ni₇ compound have been measured at temperatures of 298, 323 and 348 K, as shown in Fig. 10a, and Van't Hoff plots based on the P – C isotherms are shown in Fig. 10b.

Two plateaus are visible on each P – C curve at each temperature for hydrogen absorption and desorption. The two plateaus can be divided to the regions at a lower concentration H₂ and a higher concentration H₂, respectively. The hydrogen absorption and desorption plateau pressures of the lower plateau at the lower concentration H₂ are 0.23 and 0.15 MPa at 298 K, respectively. The hydrogen absorption and desorption plateau

pressures of the higher plateau at the higher concentration H₂ are 0.68 and 0.61 MPa at 298 K, respectively. Based on the mid-point pressures at different temperatures, the enthalpy change (ΔH) and entropy change (ΔS) of the two plateaus are respectively calculated according to the Van't Hoff equation (Fig. 10b). The hydrogenation and dehydrogenation enthalpies are determined to be -26.7 and $25.2 \text{ kJ mol}^{-1} \text{ H}_2$ for the lower plateau, and -24.5 and $22.9 \text{ kJ mol}^{-1} \text{ H}_2$ for the higher plateau, respectively (Table 2), and hydrogenation and dehydrogenation entropies are determined to be -96.6 and $87.7 \text{ J K}^{-1} \text{ mol}^{-1} \text{ H}_2$ for the lower plateau, and -97.9 and $88.8 \text{ J K}^{-1} \text{ mol}^{-1} \text{ H}_2$ for the higher plateau, respectively. Besides, the higher plateau shows superior reversibility than the lower plateau, which the hysteresis H_f at 298 K, defined as $\ln P_a/P_d$, are 0.11 and 0.45, respectively.

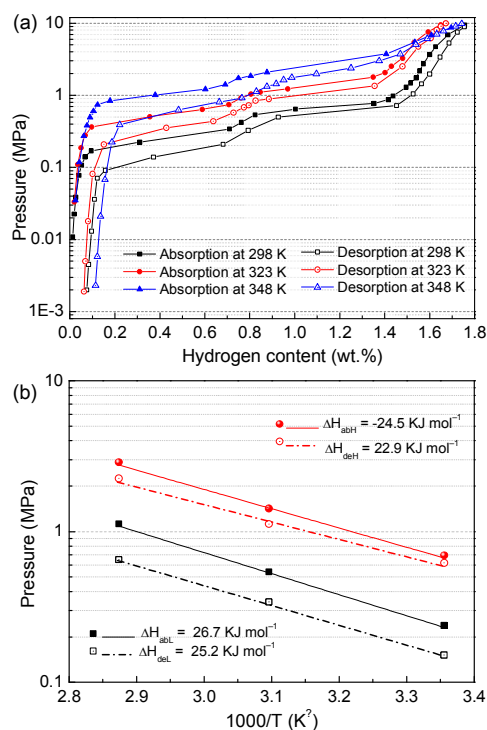


Fig. 10 Sm_{1.6}Mg_{0.4}Ni₇–H₂ system: P – C isotherms for hydrogen absorption and desorption (a), Van't Hoff plots $\log P \text{ H}_2$ vs. $1000/T$ (b).

To further verify the changes of ΔH , differential scanning calorimetry (DSC) was performed on the Sm_{1.6}Mg_{0.4}Ni₇ compound to measure the ΔH of hydrogenation and dehydrogenation. ΔH was calculated by integrating the DSC peaks shown in Fig. 11a and listed in Table 2. Upon heating, two endothermic events with the onset temperatures near 333 and 403 K are observed, and they are due to the hydrogen desorption of the hydrogenated sample. The dehydrogenation enthalpies ΔH are calculated to 21.0 and $23.0 \text{ J g}^{-1} \text{ H}_2$ (27.8 and $30.4 \text{ kJ mol}^{-1} \text{ H}_2$), respectively. During cooling, two exothermic signals are observed at 400 and 340 K, which are related to the hydrogen absorption of the sample. The hydrogenation enthalpies ΔH are calculated to -20.8 and $-17.6 \text{ J g}^{-1} \text{ H}_2$ (27.5 and $23.3 \text{ kJ mol}^{-1} \text{ H}_2$), respectively. As shown in Fig. 10, the hydrogen

desorption pressure of the higher plateau is ca. 4 times than that of the lower plateau. During the heating process, the dehydrogenation pressure of the sample and the hydrogen pressure of the sample room both increase with the increasing temperature, but the former one increases faster than the later one. When the atmosphere hydrogen pressure increases to the value below to the higher plateau dehydrogenation pressure of the sample, the hydrogen desorption process begins for the higher plateau (near 333 K). But the hydrogen desorption for the lower plateau appears much later with the rising temperature, because of the significant lower dehydrogenation pressure for the lower plateau, which needs more time as the atmosphere hydrogen pressure is further below to the dehydrogenation pressure of the lower plateau. Therefore, the dehydrogenation process of the sample exhibits two endothermic behaviors. The two endothermic peaks belong to the higher and lower plateaus during heating process, respectively. The hydrogen absorption process during cooling process exhibits two exothermic peaks with the same reason and the two peaks relate to the lower and higher plateaus, respectively. Based on the analysis of the DSC curves, it can be seen that the calculated hydrogenation enthalpies for the lower and higher plateaus are close to PCT measurements, but the dehydrogenation enthalpies are a little higher than the values from PCT measurements, which may be relevant to the heating rate. Besides, it can be noticed that the endothermic and exothermic peaks for the lower plateau show overlapped peaks with two peak-values (magnified and fitted as Fig. 11b and c), differing from the peaks for the lower plateau. This is closely related to the hydrogenation and dehydrogenation process, which will be discussed later.

3.6. Hydrogen absorption–desorption process

To determine the reaction during the two plateau courses, the structural changes of the $\text{Sm}_{1.6}\text{Mg}_{0.4}\text{Ni}_7$ compound during hydrogen absorption and desorption processes are analyzed. Although the equilibrium pressures of hydrogen absorption and desorption are fairly higher than 0.1 MPa at 25 °C for the $\text{Sm}_{1.6}\text{Mg}_{0.4}\text{Ni}_7$ compound, however the hydrogen in the compound bulk did not decompose and release under ambient condition as can be seen in Fig. 12, which the peaks of Gd_2Co_7 - (3R) and Ce_2Ni_7 -type (2H) phases had moved correspondingly to lower and higher angel during hydrogen absorption and desorption, respectively.

As shown in Fig. 12a, three processes can be exacted: when the hydrogen content at 0.06 and 0.10 wt%, the peaks of the 2H and 3R

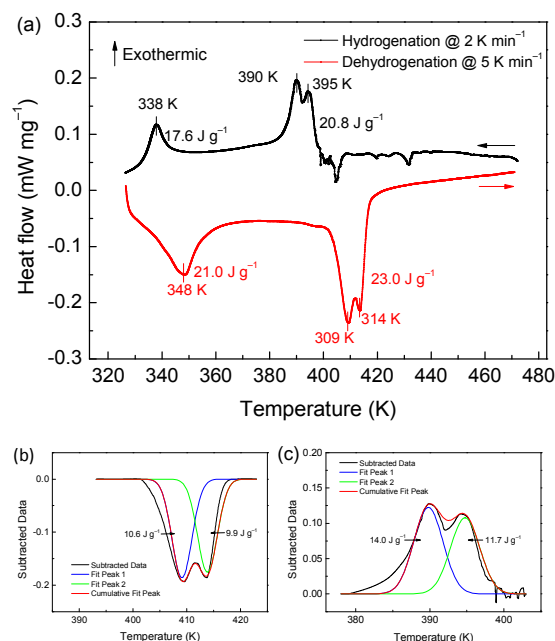


Fig. 11 DSC curves of the $\text{Sm}_{1.6}\text{Mg}_{0.4}\text{Ni}_7$ compound for the hydrogenation and dehydrogenation under 3MPa hydrogen pressure (a). Fitting results of the overlapping peaks for dehydrogenation (b) and hydrogenation (c).

phases move to lower angel without peak broadening and keep original shapes. When the hydrogen content increases from 0.31 to 0.71 wt%, except for the original peaks of the 2H and 3R phases, broaden peaks of the 2H and 3R phases are significantly observed left besides the original sharp peaks. However, because the content of 2H phase is much less than that of the 3R phase, broaden peaks of the 2H phase is not so clear as those of the 3R phase until the hydrogen content increases to 0.52 wt% ($2\theta = 31.6^\circ$). As the hydrogen content further increases to 0.82 wt%, the bragg peaks abruptly sharpen again but change in shape at the 2θ range at ca. 40° and 46° , and then further move to lower angel with the new shape until to be fully hydrogenated with the 1.81 wt%. Hydrogen desorption follows the reverse process, as shown in Fig. 12b.

For hydrogen storage compounds, hydrogen absorption is accompanied with the phase transformation from H-dissolved solid solution phase to full hydride phase, and the hydrogen desorption follows the reverse process. And the transformation in the hydrogen of different states leads to appearance of hydrogenation and dehydrogenation plateaus in the $P-C$ isotherms. Generally, ternary RE–Mg–Ni compounds with superlattice structures are found to have one plateau, corresponding to the conversation of H-dissolved solid solution phase (α phase) to full hydride phase (β phase), such as the La_2MgNi_9 ,²⁹ $\text{Sm}_3\text{MgNi}_{14}$,¹¹ $\text{Nd}_{1.5}\text{Mg}_{0.5}\text{Ni}_7$ ³⁰ and $\text{La}_4\text{MgNi}_{19}$,³¹ etc.. However, for some binary compounds, such as the RE_2Ni_7 ³² and RE_2Co_7 ^{19,33} compounds, two plateaus are shown in the $P-C$ curves, which undergoes the $\alpha \leftrightarrow \beta$ - and $\beta \leftrightarrow \gamma$ -phase transformations during the lower and higher plateaus.^{21,33} Cao *et al.* found that two kinds of hydrides with different structure patterns in the XRD analysis formed at the lower and higher ones respectively ($\text{Sm}_2\text{Co}_7\text{H}_{2.9}$ and

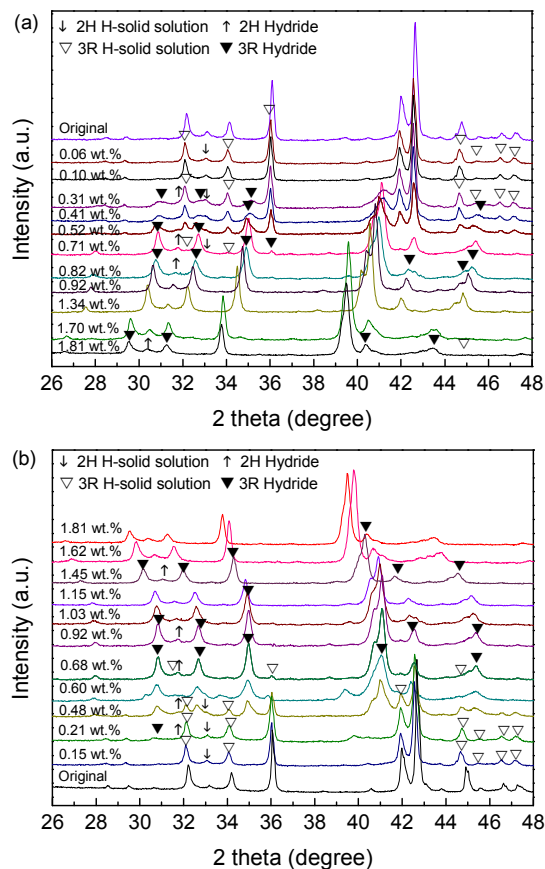


Fig. 12 XRD patterns of the $\text{Sm}_{1.6}\text{Mg}_{0.4}\text{Ni}_7$ compound during hydrogen absorption (a) and desorption (b).

$\text{Sm}_2\text{Co}_7\text{H}_{6.4}$) corresponding to the β and γ phases, respectively.¹⁹ In our study, related the P - C curves of the compound in Fig. 10 to XRD evolution with increase of H_2 content in Fig. 12, it can be determined that no γ -phase appears during the higher plateau region, because the XRD pattern of the hydride phase at the higher plateau region is in same with that of the hydride phase at the lower plateau region after transformation of H-dissolved solid solution phase. Therefore, the above three hydrogenation processes present the progress of hydrogen in solid solution phase (α -phase), corresponded to slope region at lower hydrogen content, the solid solution and hydride phases (α -phase + β - phase), related to the lower broad plateaus regions, and hydride phase (β -phase), corresponded to the higher broad plateaus region and slope region at higher hydrogen content, respectively. The dehydrogenation obeys the reverse processes. The hydrogenation and dehydrogenation processes are different from the reported the hydrogen storage compounds.

Based on absorbed hydrogen contents obtained from P - C runs, the creating β -phase hydrides for the lower and higher plateaus are calculated to be $\text{Sm}_{1.6}\text{Mg}_{0.4}\text{Ni}_7\text{H}_{4.8}$ and $\text{Sm}_{1.6}\text{Mg}_{0.4}\text{Ni}_7\text{H}_{9.0}$, respectively (Table 2). The two hydrides are with the same structure type in view of the same diffraction peaks, but in different thermodynamic stability in regards to the unlike enthalpy changes.

Studies found that hydrogen atoms in crystal lattice can occupy both the tetrahedral and octahedral sites,²¹ but the two sites exhibited different thermodynamic stabilities, which the octahedral sites are more stable than those of the tetrahedral sites. Hence, the formation of the two kinds of β -phase hydrides ($\text{Sm}_{1.6}\text{Mg}_{0.4}\text{Ni}_7\text{H}_{4.8}$ and $\text{Sm}_{1.6}\text{Mg}_{0.4}\text{Ni}_7\text{H}_{9.0}$) may closely related to the different location for entrance of hydrogen atoms with increase of H_2 concentration. And the hydrogen absorption process of the Gd_2Co_7 -type $\text{Sm}_{1.6}\text{Mg}_{0.4}\text{Ni}_7$ compound may be as follows: hydrogen atoms firstly enter into the octahedral sites of the Gd_2Co_7 -type structure with the $R\text{-}3m$ space group during the hydrogenation, forming a stable hydride $\text{Sm}_{1.6}\text{Mg}_{0.4}\text{Ni}_7\text{H}_{4.8}$ with higher enthalpy changes. After the octahedral sites are fully occupied, the hydrogen atoms further enter into the unstable tetrahedral sites, forming the $\text{Sm}_{1.6}\text{Mg}_{0.4}\text{Ni}_7\text{H}_{9.0}$ hydride with less stability after the lower reaction enthalpy change. Besides, the development of the $\text{Sm}_{1.6}\text{Mg}_{0.4}\text{Ni}_7\text{H}_{9.0}$ hydride is without the appearance of the H-dissolved solid solution phase as that of the $\text{Sm}_{1.6}\text{Mg}_{0.4}\text{Ni}_7\text{H}_{4.8}$. Therefore, it can be deduced that the H_2 directly react to the $\text{Sm}_{1.6}\text{Mg}_{0.4}\text{Ni}_7\text{H}_{9.0}$ hydride phase after decomposition to atoms based on the $\text{Sm}_{1.6}\text{Mg}_{0.4}\text{Ni}_7\text{H}_{4.8}$ compound. The DSC analysis in Fig. 11 proves the two step modes for the hydrogenation/dehydrogenation of the $\text{Sm}_{1.6}\text{Mg}_{0.4}\text{Ni}_7$ compound. As above DSC analysis, the single and overlapped endothermic peaks belong to the higher and lower plateaus, respectively. That is the single and overlapped endothermic peaks are due to the hydrogen desorption of $\text{Sm}_{1.6}\text{Mg}_{0.4}\text{Ni}_7\text{H}_{9.0}$ and $\text{Sm}_{1.6}\text{Mg}_{0.4}\text{Ni}_7\text{H}_{4.8}$ hydrides (Fig. 11a). During the dehydrogenation of $\text{Sm}_{1.6}\text{Mg}_{0.4}\text{Ni}_7\text{H}_{4.8}$, the peak at 309 K is caused by the phase transformation from hydride phase to the H-dissolved solid solution phase, and the peak at 314 K is as a result of the hydrogen releasing from the H-dissolved solid solution phase, respectively. The enthalpy changes ΔH of the two transformation processes of H_2 are calculated to be 10.6 and 9.9 $\text{J g}^{-1} \text{H}_2$ (14.0 and 13.1 $\text{kJ mol}^{-1} \text{H}_2$), respectively, which are obtained by fitting the peaks after separation of the overlapped peaks (Fig. 11b). However, the dehydrogenation process of $\text{Sm}_{1.6}\text{Mg}_{0.4}\text{Ni}_7\text{H}_{9.0}$ shows one endothermic peak, differing from the dehydrogenation process of the $\text{Sm}_{1.6}\text{Mg}_{0.4}\text{Ni}_7\text{H}_{4.8}$ hydride, which indicates that H-dissolved solid solution phase does not appear. Besides, the small hysteresis value also confirms the deduction, which large hysteresis is accompanied the formation of hydride from the H-solid solution.³⁴

Table 2 Thermodynamic and kinetic data for the $\text{Sm}_{1.6}\text{Mg}_{0.4}\text{Ni}_7$ -H system

	Lower plateau	Higher plateau
Transformation of H_2	H-solid solution (α -phase) to hydride (β -phase)	H_2 to hydride (β -phase)
Hydride	$\text{Sm}_{1.6}\text{Mg}_{0.4}\text{Ni}_7\text{H}_{4.8}$	$\text{Sm}_{1.6}\text{Mg}_{0.4}\text{Ni}_7\text{H}_{9.0}$
P_{Amin} @ 298 K (MPa)	0.23	0.68
P_{Dmin} @ 298 K (MPa)	0.15	0.61
H_{f} @ 298 K	0.45	0.11
ΔH_{A} (kJ mol^{-1}) ^a	-26.7	-24.5
ΔH_{D} (kJ mol^{-1}) ^a	25.2	22.9
ΔH_{A} (kJ mol^{-1}) ^b	-27.5	-23.3
ΔH_{D} (kJ mol^{-1}) ^b	30.4	27.8
Hydrogenation time reach 90% H_{max} @ 298 K (min)	11	1.5

^a Calculated based on the P - C isotherms

^bCalculated based on the DSC analysis

Since a difference in thermodynamic stability exists between the two plateaus, it is also important to determine the difference existed in the kinetic properties of the two plateaus. Fig. 13a and b show the hydrogen absorption rate of the lower and higher plateaus at 298 K, respectively. 90% hydrogen absorbed across the upper plateau is 1.5 min whereas 11 min is required for the same fraction of hydrogen to absorb across the lower plateau under identical conditions (Table 2). And the same result is also can be seen for the hydrogen desorption process in the Supplementary Information Fig. S1†, which the hydrogen desorption times for the lower and the upper plateaus are 7.6 and 1.2 min. The results indicate that the hydrogen absorption and desorption reaction rates across the upper plateau are ca. 7 and 6 times than those of the lower plateau, respectively.

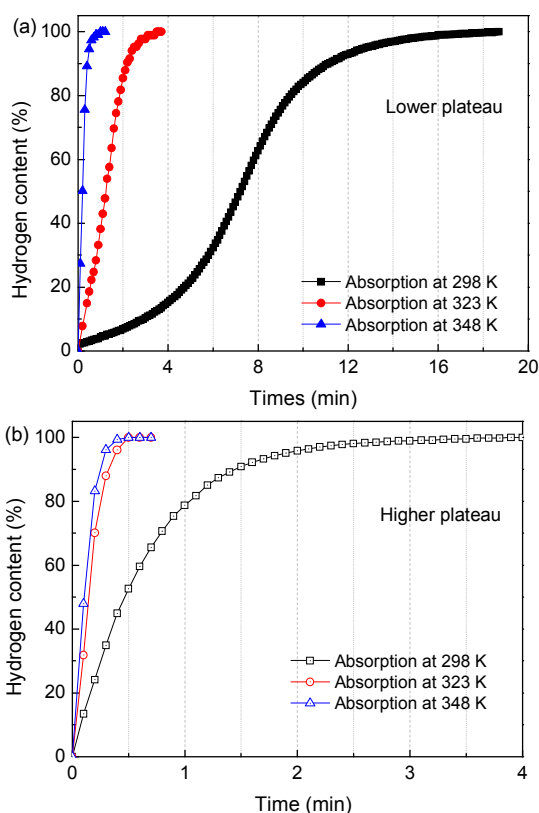


Fig. 13 Hydrogen absorption kinetic curves for the $\text{Sm}_{1.6}\text{Mg}_{0.4}\text{Ni}_7$ compound across the lower and higher plateaus measured in the range of 298–348 K.

3.7. Effect of hydrogen absorption and desorption on lattice structure

To understand the effect of the hydrogen absorption and desorption on lattice structure of the Gd_2Co_7 -type $\text{Sm}_{1.6}\text{Mg}_{0.4}\text{Ni}_7$ compound, the subunit volume changes and lattice strain during the hydrogen absorption and desorption processes are calculated and extracted to Fig. 14 based on the Rietveld refinement analysis

(Rietveld refinement images are shown in Fig. S2† and S3†). For h-

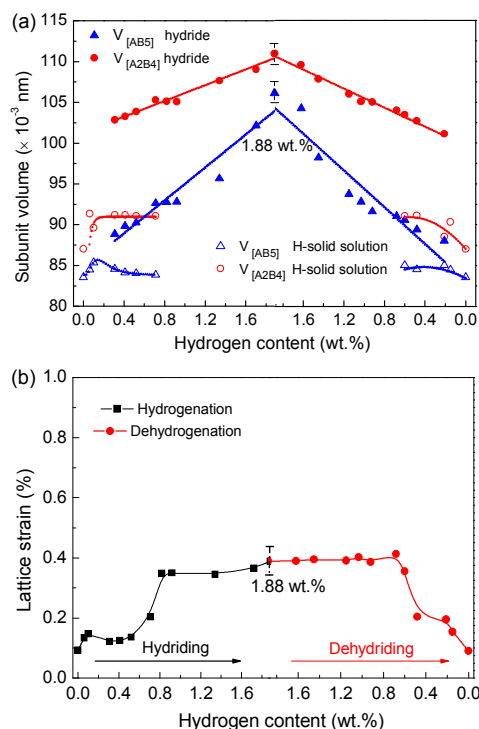


Fig. 14 Subunit volumes of the $[\text{A}_2\text{B}_4]$ and $[\text{AB}_5]$ subunits during hydrogenation and dehydrogenation of the $\text{Sm}_{1.6}\text{Mg}_{0.4}\text{Ni}_7$ compound (a). The lattice strain of the structure during hydrogenation and dehydrogenation of the $\text{Sm}_{1.6}\text{Mg}_{0.4}\text{Ni}_7$ compound (b).

-hydrogen absorption process, as shown in Fig. 13a, the volumes of $[\text{A}_2\text{B}_4]$ and $[\text{AB}_5]$ subunits change little in the α -phase with the increasing H_2 content, and the mismatch between the two subunits, which is defined as $V_{[\text{A}_2\text{B}_4]} - V_{[\text{AB}_5]}$, is ca. 5 \AA^3 . The lattice strain cause by entrance of H_2 is no more than 0.15% when H_2 is only in α -phase state. While, as the α -phase begins to transform to β -phase, the $[\text{A}_2\text{B}_4]$ subunit volume rapidly expands by 11.7 \AA^3 and that for the $[\text{AB}_5]$ subunit is 4.3 \AA^3 , and the mismatch between the two subunits in β -phase reaches 14 \AA^3 at this moment. Meanwhile, as the α -phase continuously transforms to β -phase, the mismatch between the two subunits in β -phase reduces slightly to 12.7 \AA^3 , but the lattice strain gradually increases to 0.35% with the rising content of H_2 . Besides, when the α -phase disappears and the H_2 directly forms β -phase with increasing content of H_2 , the mismatch value is significantly reduced to 4.86 \AA^3 at the maximum content of H_2 and the inner-molecular strain almost keeps constant around 0.35% during the direct conversion process of H_2 . The above results indicate that the H_2 firstly forms hydride in the $[\text{A}_2\text{B}_4]$ subunit and then in the $[\text{AB}_5]$ subunit accounting on the decreasing mismatch of the two subunits in hydride phase. And the lattice internal strain is caused from the transformation of H_2 from the H-solid solution phase to the hydride phase stage, which the transformation of H induced the expansion of the $[\text{A}_2\text{B}_4]$ subunit but constrained by the connected $[\text{AB}_5]$ subunit at the basal plane, which gives rise to a significant lattice strain. The

lattice strain increases due to continuous rising content of the hydride phase through the above process, but cannot be released with the decrease of the mismatch between the two subunits since the formed deformation for the lattice structure during direct conversion of H₂ to the hydride phase. For dehydrogenation process, the same phenomenon can be also seen in Fig. 14b and c. Besides, we also found that the lattice internal strain of the Gd₂Co₇-type Sm_{1.6}Mg_{0.4}Ni₇ compound is much smaller in comparison with the La–Mg–Ni compounds during hydrogen absorption and desorption processes.^{7,12} For example, the maximum lattice strain is reported to be 0.67% and 0.86% for the Ce₂Ni₇-type La_{1.5}Mg_{0.5}Ni₇ compound during hydrogen absorption and desorption processes, respectively. The reason of the large lattice inner strain for La–Mg–Ni compounds may be that the transformation stage between α - and β -phase is much longer. However, the transformation process between α - and β -phase for the Gd₂Co₇-type Sm_{1.6}Mg_{0.4}Ni₇ compound is shortened, which the lattice strain dose not further increase for the direct conversion between H₂ and β -phase, thus resulting in less lattice strain of the compound, and exhibiting good structural and cycling stabilities.

4. Conclusions

In this paper, we prepared a new Gd₂Co₇-type Sm_{1.6}Mg_{0.4}Ni₇ compound by powder sintering method. The Gd₂Co₇-type Sm_{1.6}Mg_{0.4}Ni₇ compound is found to be with good hydrogen storage ability and have special hydrogen absorption/desorption process. The compound can be activated at the 1st cycle and absorb 1.88 wt% H₂ within 17 min at 298 K under 10 MPa H₂ after activation. And the hydrogen absorption speed increases to 3.4 min after 20 absorption/desorption cycles with a 1.44 wt% H₂ under 3 MPa H₂. Especially, 99.3% of the maximum hydrogen storage capacity is hold for the Gd₂Co₇-type Sm_{1.6}Mg_{0.4}Ni₇ compound at the 100th cycle. The hydrogen absorption/desorption of the Gd₂Co₇-type Sm_{1.6}Mg_{0.4}Ni₇ compound undergoes two equilibrium stages and exhibiting two plateaus in the P–C curves. At the lower concentration H₂ stage, H₂ transforms between H-solid solution phase and hydride phase with a lower rate and higher enthalpy change in lower pressure, and at the higher concentration H₂ stage, H₂ directly converts between atom states and the hydride phase with a higher rate and lower enthalpy change in higher pressure. We found the transformation of H₂ at the lower concentration of H₂ stage results in inner-molecular strain and mismatch in subunit volumes in hydrogenation/desorption, and the shorten lower concentration of H₂ stage in the two step mode lowers the inner-molecular strain and mismatch in subunit volumes of the compound, thus leading to good structural stability and excellent cycling stability. These findings are expected to provide an important guidance for developing viable intermetallic materials as high-pressure tank materials for hydrogen storage with nice hydrogen storage properties.

Acknowledgment

This work was financially supported by the National Natural Science Foundation of China (NO. 51571173), the Natural Science Foundation of Hebei Province (NO B2014203114), the Innovation

Fund for the Graduate Students of Hebei Province (NO. 00302-6370014) and Plan for Scientific Innovation Talent of Henan Province (NO 144100510009).

References

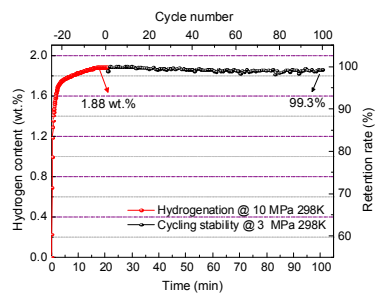
- 1 K. Young and J. Nei, *Materials*, 2013, **6**, 4574.
- 2 Y. F. Liu, H. G. Pan, M. X. Gao and D. Q. Wang, *J. Mater. Chem.*, 2011, **21**, 4743.
- 3 A. A. Volodin, C. B. Wan, R. V. Denys, G. A. Tsirlina, B. P. Tarasov, M. Fichtner, U. Ulmer, Y. D. Yu, C. C. Nwakwuo and V. A. Yartys, *Int. J. Hydrogen Energy*, 2016, in press.
- 4 R. V. Denys, A. B. Riabov, V. A. Yartys, M. Sato and R. G. Delaplane, *J. Solid State Chem.*, 2008, **181**, 812.
- 5 V. Yartys and R. Denys, *J. Alloys Compd.*, 2015, **645**, S412.
- 6 C. B. Wan, R. V. Denys and V. A. Yartys, *J. Alloys Compd.*, 2016, **670**, 210.
- 7 Q. A. Zhang, M. H. Fang, T. Z. Si, F. Fang, D. L. Sun, L. Z. Ouyang and M. Zhu, *J. Phys. Chem. C*, 2010, **114**, 11686.
- 8 I. Park, N. Terashita and E. Abe, *J. Alloys Compd.*, 2013, **580**, S81.
- 9 K. Young, T. Ouchi, H. Shen and L. A. Bendersky, *Int. J. Hydrogen Energy*, 2015, **40**, 8941.
- 10 Z. L. Chen, T. Z. Si and Q. A. Zhang, *J. Alloys Compd.*, 2015, **621**, 42.
- 11 Q. A. Zhang, Z. L. Chen, Y. T. Li, F. Fang, D. L. Sun, L. Z. Ouyang and M. Zhu, *J. Phys. Chem. C*, 2015, **119**, 4719.
- 12 J. J. Liu, Y. Li, D. Han, S. Q. Yang, X. C. Chen, L. Zhang and S. M. Han, *J. Power Sources*, 2015, **300**, 77.
- 13 L. Zhang, Y. Li, X. Zhao, J. J. Liu, D. D. Ke, W. K. Du, S. Q. Yang and S. M. Han, *J. Mater. Chem. A*, 2015, **3**, 13679.
- 14 J. J. Liu, S. M. Han, D. Han, Y. Li, S. Q. Yang, L. Zhang and Y. M. Zhao, *J. Power Sources*, 2015, **287**, 237.
- 15 L. Zhang, S. M. Han, Y. Li, J. J. Liu, J. L. Zhang, J. D. Wang and S. Q. Yang, *Int. J. Hydrogen Energy*, 2013, **38**, 10431.
- 16 L. Zhang, S. M. Han, D. Han, Y. Li, X. Zhao and J. J. Liu, *J. Power Sources*, 2014, **268**, 575.
- 17 W. Ostertag, *J. Less-Common Met.*, 1967, **13**, 385.
- 18 R. Fersi, N. Mliki, L. Bessais, R. Guetari, V. Russier and M. Cabié, *J. Alloys Compd.*, 2012, **522**, 14.
- 19 Z. J. Cao, L. Z. Ouyang, H. Wang, J. W. Liu, D. L. Sun, Q. A. Zhang and M. Zhu, *J. Alloys Compd.*, 2014, **608**, 14.
- 20 L. Zhang, Y. Q. Ding, Y. M. Zhao, W. K. Du, Y. Li, S. Q. Yang and S. M. Han, *Int. J. Hydrogen Energy*, 2016, **41**, 1791.
- 21 L. Ming and A. J. Goudy, *J. Alloys Compd.*, 1999, **283**, 146.
- 22 K. Iwase, N. Terashita, K. Mori and T. Ishigaki, *Inorg. Chem.*, 2012, **51**, 11805.
- 23 Z. Y. Liu, X. L. Yan, N. Wang, Y. J. Chai and D. L. Hou, *Int. J. Hydrogen Energy*, 2011, **36**, 4370.
- 24 Y. M. Li, H. P. Ren, Y. H. Zhang, Z. C. Liu and H. W. Zhang, *Int. J. Hydrogen Energy*, 2015, **40**, 7093.
- 25 J. Zhang, F. Fang, S. Y. Zheng, J. Zhu, G. R. Chen, D. L. Sun, M. Latroche and A. Percheron-Guégan, *J. Power Sources*, 2007, **172**, 446.
- 26 R. C. Bowman, C. A. Lindensmith, S. Luo, T. B. Flanagan and T. Vogt, *J. Alloys Compd.*, 2002, **330**, 271.
- 27 K. Sakaki, N. Terashita, H. Kim, E. H. Majzoub, A. Machida, T. Watanuki, S. Tsunokake, Y. Nakamura and E. Akiba, *J. Phys. Chem. C*, 2014, **118**, 6697.
- 28 H. Kim, K. Sakaki, H. Ogawa, Y. Nakamura, J. Nakamura, E. Akiba, A. Machida, T. Watanuki and T. Proffen, *J. Phys. Chem. C*, 2013, **117**, 26543.
- 29 R. V. Denys and V. A. Yartys, *J. Alloys Compd.*, 2011, **509**, Supplement 2, S540.
- 30 Q. A. Zhang, B. Zhao, M. H. Fang, C. R. Liu, Q. M. Hu, F. Fang, D. L. Sun, L. Z. Ouyang and M. Zhu, *Inorg. Chem.*, 2012, **51**, 2976.

ARTICLE

Journal Name

- 31 J. Nakamura, K. Iwase, H. Hayakawa, Y. Nakamura and E. Akiba, *J. Phys. Chem. C*, 2009, **113**, 5853.
- 32 K. Iwase, K. Mori, A. Hoshikawa and T. Ishigaki, *Int. J. Hydrogen Energy*, 2012, **37**, 5122.
- 33 A. Goudy, W. E. Wallace, R. S. Craig and T. Takeshita, in: R. Bau (Ed.), *Transition Metal Hydrides Advances in Chemistry Series*, 1978, **167**, 312.
- 34 F. A. Kuijpers and H. H. van Mal, *J. Less-Common Met.*, 1971, **23**, 395.

Table of contents



The Gd₂Co₇-type Sm_{1.6}Mg_{0.4}Ni₇ compound can absorb 1.881 wt.% H₂ and retain 99.3% the initial hydrogen content after 100 cycles